Research Article

Nano Biomed Eng

Donor–Acceptor–Donor Structured Dyes with Balanced Photothermal Conversion Efficiency and Fluorescence Quantum Yield for Near-Infrared–II Mild-Temperature Photothermal Therapy

Xuan Sun[1,§], Zuyuan Zhang[1,§], Chunbai Xiang[3,§], Tianhe Qiao[1], Xin Wang[1] ✉, Gongcheng Ma[4] ✉, Dan Ding[2] ✉

[1] The First Department of Breast Cancer, Tianjin Medical University Cancer Institute and Hospital, National Clinical Research Center for Cancer, Key Laboratory of cancer Prevention and Therapy, Tianjin's Clinical Research Center for Cancer and Key Laboratory of Breast Cancer Prevention and Therapy, Tianjin Medical University, Ministry of Education, Tianjin 300060, China
[2] Frontiers Science Center for New Organic Matter, Engineering & Smart Sensing Interdisciplinary Science Center, MOE Key Laboratory of Bioactive Materials, and college of Life Sciences, Nankai University, Tianjin 300350, China
[3] Key Laboratory of Green Chemistry and Technology (Ministry of Education), College of Chemistry, Sichuan University Chengdu 610064, China
[4] School of Life Science and Technology, Xinxiang Medical University, Xinxiang 453003, China

[§] These authors contributed equally to this work.

✉ Corresponding authors. E-mails: Xin Wang, wangxin@tjmuch.com; Gongcheng Ma, mgc_lc@163.com; Dan Ding, dingd@nankai.edu.cn

Received: Feb. 13, 2025; **Revised:** Mar. 3, 2025; **Accepted:** Mar. 7, 2025

Citation: X. Sun, Z.Y. Zhang, C.B. Xiang, et al. Donor–acceptor–donor structured dyes with balanced photothermal conversion efficiency and fluorescence quantum yield for near-infrared–II mild-temperature photothermal therapy. *Nano Biomedicine and Engineering*, 2025, 17(2): 248−262.
http://doi.org/10.26599/NBE.2025.9290120

Abstract

Effective mild-temperature photothermal therapy (MTPTT) requires photothermal agents with high photothermal conversion efficiency (PCE) and balanced fluorescence quantum yield to enable efficient tumor treatment while minimizing damage to surrounding healthy tissues. In this study, we designed donor–acceptor–donor structured dyes, 4,4'-((6,7-di(thiophen-2-yl)-[1,2,5]thiadiazolo[3,4-g]quinoxaline-4,9-diyl)bis(thiophene-5,2-diyl))bis(N,N-bis(4-methoxyphenyl)aniline) (IT-STPA) and 4,4'-((6,7-di(furan-2-yl)-[1,2,5]thiadiazolo[3,4-g]quinoxaline-4,9-diyl)bis(thiophene-5,2-diyl))bis(N,N-bis(4-methoxyphenyl)aniline) (IT-OTPA), featuring furan-modified thiadiazolo-quinoxaline for near-infrared–II (NIR-II) fluorescence imaging and enhanced PCE. The furan and thiophene modifications promoted aggregation-induced emission, resulting in strong fluorescence emission (1 000–1 400 nm) while maintaining a high PCE of 48.5%. IT-OTPA was encapsulated into nanoparticles for improved aqueous dispersion and combined with the HSP70 inhibitor apoptozole (APZ) to form OTAPZ nanoparticles. The efficacy of this combination was evaluated both *in vitro* and *in vivo*, showing efficient tumor targeting and effective MTPTT under NIR laser irradiation. This study presents a promising approach for enhancing MTPTT through balanced photothermal and fluorescence properties, offering new possibilities for cancer treatment.

Keywords: mild-temperature photothermal therapy; photothermal conversion efficiency; near-infrared–II imaging; heat shock protein

Introduction

Mild-temperature photothermal therapy (MTPTT) has emerged as an effective treatment modality for cancer, enabling targeted tumor ablation while minimizing damage to healthy tissues. To enhance the therapeutic efficiency of MTPTT, photothermal agents with high photothermal conversion efficiency (PCE) and robust fluorescence properties are required for accurate tumor localization and real-time treatment monitoring [1–6]. However, maintaining a balance between high PCE and fluorescence quantum yield (FQY) is challenging [7] because an excessive PCE may reduce the fluorescence emission and vice versa. Thus, the development of photothermal agents capable of achieving efficient thermal conversion and optimal fluorescence emission is essential for improving the therapeutic and diagnostic performance of MTPTT. Phototheranostic agents, which integrate fluorescence imaging (FLI) with MTPTT, enable tumor targeting and monitoring with enhanced precision, providing a robust treatment approach for cancer [8–12]. Recent advancements have focused on organic photosensitizers, particularly aggregation-induced emission (AIE) materials and small organic molecules, which are capable of emitting light in the near infrared–II (NIR-II) region [13]. These materials are preferred because of their deeper tissue penetration, reduced scattering, superior signal-to-background ratio, and good biocompatibility [14–17]. To achieve high PCE, these agents should be optimized for the efficient conversion of light into heat while simultaneously maintaining strong fluorescence emission, thereby allowing effective tumor imaging. The simultaneous enhancement of both properties ensures not only the efficacy of photothermal therapy (PTT) but also the precise monitoring of treatment progress. A promising strategy to achieve this balance is the design of small organic molecules with a donor–acceptor–donor (D–A–D) structure [18]. The D–A–D architecture enables the precise tuning of molecular electronic properties, such as absorption and emission wavelengths, which directly influence the PCE and FQY. Owing to their clear chemical designs, tunable optical properties, and excellent metabolic profiles, organic small molecules with a D–A–D structure are a key focus of research on molecular design in PTT and imaging [19–22].

In this study, we conceived and synthesized two small molecules with a D–A–D structure (IT-STPA and IT-OTPA) based on IT-PA to achieve a balance between high PCE and FQY. The introduction of thiophene into IT-STPA and furan into IT-OTPA considerably improved the PCE while maintaining a high fluorescence strength in the NIR-II region [23–26]. The furan-modified thiadiazolo-quinoxaline core of IT-OTPA ensured excellent photothermal efficiency and fluorescence performance. To further optimize this balance, IT-OTPA was encapsulated into nanoparticles, and the resulting OT NPs were combined with the HSP70 inhibitor APZ to form OTAPZ NPs. The therapeutic efficacy and FLI capabilities of the OTAPZ NPs were evaluated *in vitro* and *in vivo*, demonstrating their potential for MTPTT and fluorescence-guided imaging for enhanced cancer treatment (Scheme 1).

Experimental

Synthesis and characterization of IT-STPA and IT-OTPA

Details about the synthesis process and characterization data are provided in the Electronic Supplementary Material (ESM).

Materials

Chemicals and solvents were provided by commercial suppliers, including TCI, J&K, and Sigma-Aldrich, and used as received without any additional purification. Dichloromethane, tetrahydrofuran (THF), and toluene solvents were purchased from Nanjing Reagent and dried and purified by passing through columns filled with alumina and Q5 reactant on a solvent purification system. All reactions sensitive to air and moisture were conducted in glassware dried by flame under argon atmosphere.

Photothermal measurement

OTAPZ NP aqueous solutions were prepared using fluorophore at concentrations ranging from 6.25 to 100 μmol/L. Then, using deionized water as the control, these solutions were continuously irradiated with an 808-nm laser at preset power densities for 4 min. The temperature was recorded using an infrared thermal camera.

PCE calculation

The PCEs (η) of IT-PA, IT-STPA, and IT-OTPA in

dimethylsulfoxide (DMSO) solution were determined according to the literature. The DMSO solutions were irradiated with an 808-nm laser at a power density of 1 W/cm^2 for 14 min. After laser irradiation, the solutions were allowed to cool naturally for 14 min. The temperature was recorded every 20 s using an infrared thermal camera. The PCEs (η) were calculated using the following equation:

$$\eta = \frac{hA(T_{max} - T_{surr}) - Q_{dis}}{(1 - 10^{-A_{808}})} \quad (1)$$

where h is the heat transfer coefficient, A is the surface area of quartz plate, T_{max} is the maximum steady-state temperature, T_{surr} is the temperature of the surrounding environment, and Q_{dis} is the irradiation heat dissipated from the solvent and container.where I represents the laser power, A_{808} is the absorbance of the sample at 808 nm.

Furthermore, Q_{dis} can be calculated using the following equation:

$$Q_{dis} = \frac{m_D C_D \left(T_{maxt(water)} - T_{surr}\right)}{\tau_{S(water)}}$$
$$\tau_S = \frac{m_D C_D}{h_A} \quad (2)$$

where m_D and c_D are the mass and heat capacity (4.2 J/g) of the deionized water used to dissolve the photothermal agents. τ_s denotes the time constant of heat transfer.

Photothermal stability studies

ICG(Indocyanine Green) and OTAPZ NPs were irradiated with an 808-nm laser (1 W/cm^2) in aqueous solutions (100 μmol/L) for 15 min, and the absorption spectra were recorded at 5 and 15 min. For antiphotobleaching assessment, the ICG and OTAPZ NP solutions (100 μmol/L) were irradiated with an 808-nm laser (1 W/cm^2) for 3 min until thermal equilibrium was reached. Then, the laser was turned off, and the solutions were allowed to cool at room temperature(25 °C) for 4 min. This heating–cooling process was performed five times while measuring the solution temperature every 15 s using an infrared thermal imaging camera.

Preparation of OTAPZ NPs

To prepare OTAPZ NPs, ICG (0.87 mg), APZ (1 mg), and DSPE-PEG2000 (4 mg) were jointly dissolved in 1 mL of THF. Next, this solution was added dropwise to 10 mL of deionized water and was ultrasonically mixed for 3 min. After evaporation of THF, the obtained OTAPZ NP suspension was purified using a 0.45-μm syringe-driven filter.

Cell culture

The American Type Culture Collection provided murine breast cancer cells (4T1), which were subjected to regular checks for mycoplasma contamination and cultured using RPMI-1640 medium with 10% fetal bovine serum and 1% penicillin–streptomycin. Then, the cells were maintained in a 37 °C environment under a humidified atmosphere containing 5%CO_2.

CCK8 assay

The CCK8 assay was used to evaluate the *in vitro* cytotoxicity and antitumor efficacy of APZ NPs, OT NPs, and OTAPZ NPs using the 4T1 cell line. Briefly, each well of a 96-well plate was seeded with 5 × 10^3 4T1 cells. After 24 h, the cells were treated with APZ NPs, OT NPs, and OTAPZ NPs (100 μL in RPMI-1640 medium) at concentrations ranging from 6.25 to 100 μmol/L. After 8 h of incubation, the cells were maintained either under dark conditions or exposed to an 808-nm laser (1 W/cm^2) for 3 min. After another 24 h, 10 μL of CCK8 solution (10 μL per 100 μL of culture medium) was added to each well. After incubation for 2 h, the absorbance at 490 nm was measured using a microplate reader. The cell viability was determined as a percentage relative to the control group.

Live/Dead cell staining

4T1 cells were cultured with phosphate-buffered saline (PBS) for live/dead cell staining. In confocal dishes, the cells were cultured with OT NPs, APZ NPs, and OTAPZ NPs (50 μmol/L in 1 mL of RPMI-1640) for 12 h and then either maintained under dark conditions or exposed to an 808-nm laser (1 W/cm^2) for 5 min. After 12 h, a mixture of calcein AM and propidium iodide (PI) was used to costain the cells for 45 min. Then, after two washes with PBS, 1 mL of fresh RPMI-1640 medium was added to the cells.

Western blot analysis of HSP70

For the western blot analysis of HSP70, murine 4T1 cells were seeded into a six-well plate and cultured for 24 h. Then, the cells were subjected to different treatments: (1) incubation at 37 °C cell incubator, (2) cultivation at 42 °C for 1 h before cultivating in incubator, and (3) treatment with PBS, OT NPs, APZ NPs, and OTAPZ NPs (100 μmol/L) for 8 h.

Subsequently, the different groups were irradiated with an 808-nm NIR laser for 10 min (0.8 W/cm^2) and named PBS+NIR, OT NPs+NIR, APZ NPs+NIR, and OTAPZ NPs+ NIR. Then, they were collected and disrupted via RIPA for 10 min. HSP70 expression was detected through western blot analysis using an exposure meter.

Flow cytometry analysis

Flow cytometry analysis was conducted to assess apoptosis and further evaluate the antitumor effect of PTT. The 4T1 cells were cultured in a six-well plate overnight at 37 °C under 5%CO_2. Once a confluent monolayer was formed, PBS, OT NPs, APZ NPs, and OTAPZ NPs (100 μmol/L in RPMI-1640) were added to the culture, and the cells were incubated for 8 h. The cells were divided into two sets of groups: unirradiated groups (PBS, OT NPs, APZ NPs, and OTAPZ NPs) and irradiated groups (PBS+NIR, OT NPs+NIR, APZ NPs+NIR, and OTAPZ NPs+NIR), which were exposed to an 808-nm laser (1 W/cm^2) for 3 min. After irradiation, the cells were collected by trypsinization (without EDTA), washed twice with saline (centrifuged at 1 000× *g* for 5 min), and dyed using Annexin-V-FITC kit.

Enzyme-linked immunosorbent assay (ELISA)

BALB/c mouse tumor samples were treated with PBS, OT NPs, APZ NPs, OTAPZ NPs, PBS + NIR, OT NPs + NIR, APZ NPs + NIR, and OTAPZ NPs + NIR and then ground after centrifugation. The Mouse HSP-70/HSPA9 (Heat Shock Protein 70) ELISA kit was used to detect HSP70 expression.

NIR-II FLI

BALB/c mice with tumors were first anesthetized and then administered with OTAPZ NP aqueous solutions (150 μL, 400 μmol/L) via tail vessel injection. The fluorescence signals at different time intervals were detected using a NIR-II imaging system with an 808-nm pulsed laser excitation.

In vivo experiment

The 4T1 tumor-bearing mice were randomly allocated into eight groups (n = 4 per group) and intravenously injected with PBS, PBS+NIR, OT NPs, OT NPs + NIR, APZ NPs, APZ NPs + NIR, OTAPZ NPs, and OTAPZ NPs + NIR. Each mouse was subjected to irradiation (808 nm, 0.5 W/cm^2) at the tumor region accurately. An infrared thermal imaging camera captured the image of the tumor sites and recorded the temperature every 15 s. The body weight and tumor size of mice were recorded every 2 days for 14 days. The mouse tumor volume was calculated as follows: volume = (width^2 × length)/2. On day 14, all mice in the eight groups were euthanized after performing MTPTT for histological studies. The tumors and vital organs, including the spleen, heart, lungs, liver, and kidneys, were excised, sliced, and then stained. For hematoxylin and eosin (H&E) staining, the tissues were first fixed in 4% formalin, dehydrated, embedded in paraffin, and finally sliced to a thickness of 8 μm. For Ki-67 and HSP70 staining, standard protocols for immunohistochemical (IHC) procedures were followed.

Results and Discussion

Synthesis and characterization

In this study, new electron acceptors OTPA and STPA were developed by introducing furan and thiophene into the thiadiazolo-quinoxaline core, respectively, and their properties were compared by performing quantum chemical calculations after forming D–A–D-type fluorophores with the strong donor IT.

According to the root mean square deviation calculations of the ground and excited state structures (Fig. 1(a)), the structural differences of IT-OTPA primarily arose from the triphenylamine and furan units, whereas IT-STPA exhibited differences mainly due to the incorporation of thiophene. These findings aligned with our initial design concept. The results indicated a significant deviation of 0.6604 Å in the excited state and ground-state structures of IT-OTPA, suggesting that IT-OTPA undergoes more pronounced configuration changes than IT-STPA. The highest occupied molecular orbital (HOMO) electron cloud was distributed across the entire molecular skeleton, whereas the lowest unoccupied molecular orbital (LUMO) electron cloud was predominantly localized on the receptor and thiophene units (Fig. 1(a)). This indicates that the molecule can undergo strong intramolecular charge transfer in the ground state. The HOMO energy level of the two molecules was approximately −4.75 eV, whereas the LUMO energy level was approximately −3.45 eV, with an energy level difference of approximately 1.3 eV. Upon introducing the thiophene and furan moieties, the molecular planarity

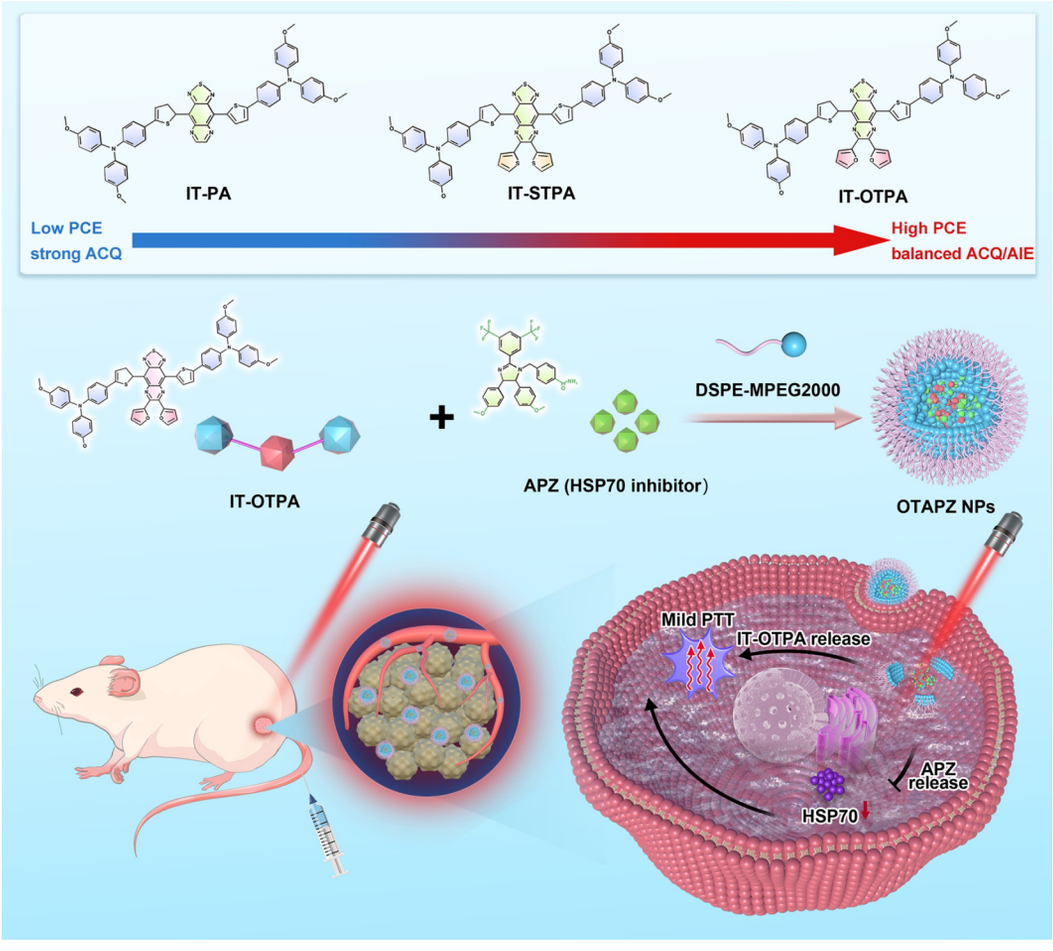

Scheme 1 Schematic of the molecular structures and properties of IT-PA, IT-STPA, and IT-OTPA. Preparation of OTAPZ NPs using IT-OTPA and APZ. Mild-temperature photothermal therapy (MTPTT) process using OTAPZ NPs.

of IT-STPA (2.8°) and IT-OTPA (3.2°) was slightly reduced compared with that of IT-PA, favoring a reduction in intermolecular π–π stacking. Nevertheless, the dihedral angles between the phenylpropyl thiadiazole unit and the thiophene unit in IT-OTPA and IT-STPA were minimal, approximately 3°, contributing to a strong planar feature [27, 28], which enhances the compound's absorption performance, yielding a high molar extinction coefficient and facilitating the redshift of the absorption and emission wavelengths, which ultimately improves the PCE in the aggregation state [29]. Meanwhile, owing to its large steric resistance, triphenylamine forms a considerable angle with the central nitrogen atom, preserving the intramolecular motion and potentially allowing for ideal nonradiative transitions.

The HOMO–LUMO bandgaps of IT-PA, IT-STPA, and IT-OTPA were calculated as 1.28, 1.318, and 1.32 eV, respectively, suggesting that the acceptor group exerted a minimal influence. Figs. 1(b) and 1(c) shows the absorbance and fluorescence intensity curves of IT-PA, IT-STPA, and IT-OTPA in THF, with their absorption/emission maxima detected at 854/1110, 823/1096, and 837/1110 nm, respectively. IT-PA exhibited the longest fluorescence wavelength, correlating with the smallest LUMO bandgap, whereas IT-STPA displayed the shortest wavelengths attributed to the largest HOMO–LUMO bandgap. As expected, IT-OTPA displayed intermediate absorbance and emission wavelengths.

To further examine the fluorescence properties of these fluorophores in the aggregation state, the emission spectra of these molecules were detected in THF/H_2O mixtures with varying water volume fractions (f_w), as shown in Fig. 1(d) and Fig. S1 in the Electronic Supplementary Material (ESM). With increasing f_w, the fluorescence intensities of IT-PA, IT-STPA, and IT-OTPA decreased, likely due to intermolecular π–π stacking in the aggregation state, which is consistent with the typical ACQ material. However, the decreases in fluorescence intensities for

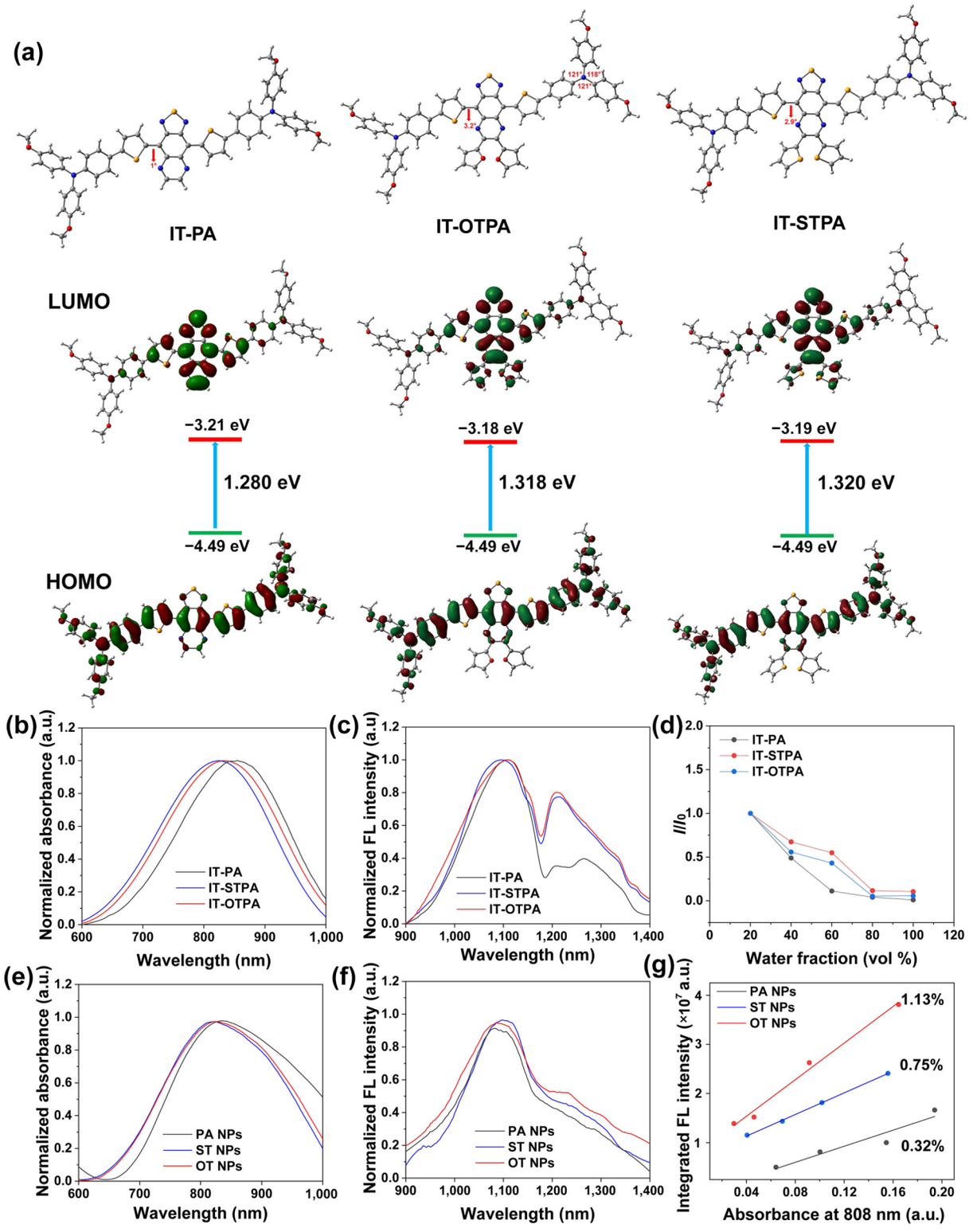

Fig. 1 (a) Optimized ground-state (S0) geometries, lowest unoccupied molecular orbitals (LUMO), and highest occupied molecular orbitals (HOMOs) of IT-PA, IT-OTPA, and IT-STPA. **(b)** and **(c)** Normalized absorption and fluorescence intensity of IT-PA, IT-STPA, and IT-OTPA. **(d)** Plot of the relative emission intensity (I/I_0) versus water volume fraction (fw), where I_0 and I are the maximum values of fluorescence intensities of the fluorophores in THF and THF/H_2O mixtures, respectively. **(e)** Normalized absorbance of nanoparticles in water. **(f)** Normalized fluorescence intensity of nanoparticles. **(g)** Plot of the integrated fluorescence intensity (900–1400 nm) of the NPs vs. the absorbance at 808 nm.

IT-STPA and IT-OTPA were less pronounced, indicating that the modification with thiophene and furan altered the molecular characteristics.

To investigate the biological imaging potential of

these fluorophores in the NIR-II region, their optical properties were examined in aqueous media. The absorption and emission spectra of IT-PA NPs, IT-STPA NPs, and IT-OTPA NPs in water are shown in Figs. 1(e) and 1(f). The strongest absorption/emission wavelengths of IT-PA NPs, IT-STPA NPs, and IT-OTPA NPs were detected at 836/1 084, 811/1 096, and 823/1 085 nm, respectively. Notably, all emission wavelengths fell within the NIR-II spectral range for each type of NPs. The FQYs of PA NPs, ST NPs, and OT NPs in the 900–1 400 nm region were 0.35%, 0.72%, and 1.13%, respectively, which can be attributed to the AIE properties of IT-STPA and IT-OTPA, as shown in Fig. 1(g).

Photophysical properties and theoretical calculations

The PCEs of IT-PA, IT-STPA, and IT-OTPA were determined to be 23.5%, 37.4%, and 48.5%, respectively (Fig. 2(a) and Fig. S7 in the ESM), indicating that IT-OTPA exhibits the best photothermal performance among the three materials. The total reorganization energy represents the energy released when the excited state returns to the ground state. This reorganization energy can be decomposed into contributions from each vibrational mode. The HR factor reflects the probability of a molecule returning to the ground state through nonradiative transitions associated with each vibrational mode. As shown in Figs. 2(b) and 2(c) and Fig. S5 in the ESM, the proportion of reorganization energy of IT-OTPA and IT-STPA in the low-frequency vibrational region (< 200 cm^{-1}) reached 42.3% and 34.6%, respectively. This suggests that the reorganization energy in these molecules is mostly concentrated in the region with a high probability of nonradiative transitions and significant energy. The vibration modes primarily involve the triphenylamine and furan or thiophene units. These results support the theoretical prediction that both IT-OTPA and IT-STPA exhibit efficient nonradiative transition pathways, contributing to their strong photothermal conversion abilities.

In addition, the calculated nonradiative transition rates of IT-OTPA and IT-STPA were 1.35×10^{11} and 1.02×10^{11} s^{-1}, respectively, which were consistent with the observed photothermal properties. Subsequently, IT-OTPA was encapsulated with the amphiphilic molecule DSPE-PEG2000 and investigated for its stability and photothermal properties. In an aqueous system, the PCE of OT NPs was measured under 808-nm laser irradiation (Fig. 2(d)). The stability of the NPs was evaluated by performing five consecutive increase-decrease cycles under 808-nm laser irradiation, and the photothermal behavior was examined at power levels ranging from 0.2 to 0.8 W (Fig. 2(e) and Fig. S6 in the ESM). The temperature increased with increasing laser power and NP concentration (Fig. 2(f)), demonstrating the excellent photothermal performance and stability of

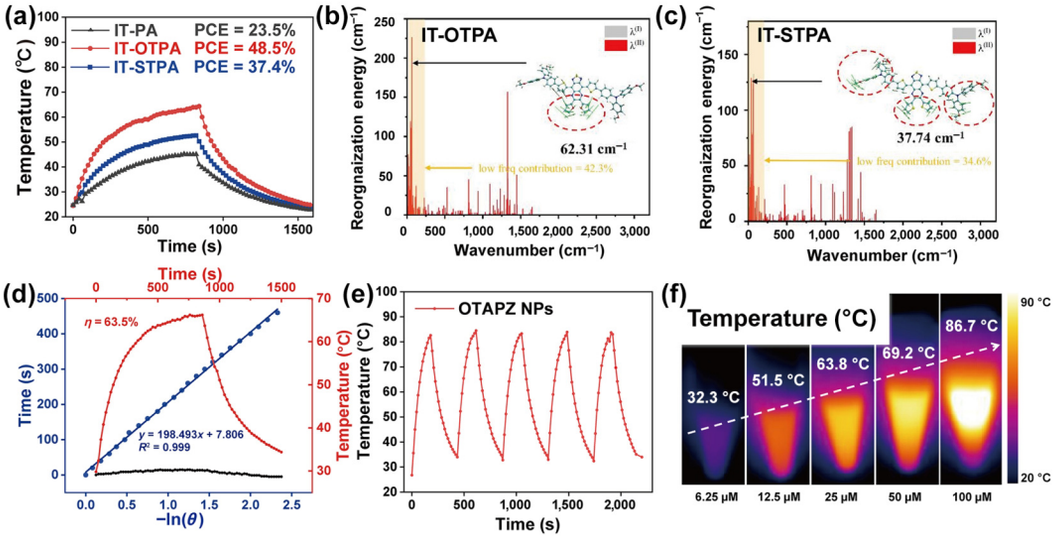

Fig. 2 Photostability and photothermal properties of IT-PA, IT-STPA, IT-OTPA, PA NPs, ST NPs, and OT NPs. **(a)** Photothermal conversion efficiency (PCE) of IT-PA, IT-STPA, and IT-OTPA (100 μmol/L) in water under continuous 808-nm laser irradiation (1 W/cm^2) for 28 min. The PCEs were 23.5%, 37.4%, and 48.5%, respectively. **(b)** and **(c)** Reorganization energy of IT-OTPA and IT-STPA. **(d)** PCE of OT NPs in water under 808-nm laser irradiation (1 W/cm^2). The PCE of OT NPs was 63.6%. **(e)** Photothermal stability of OT NPs in water (100 μmol/L) during five irradiation–cooling cycles (1 W/cm^2). **(f)** Infrared images depicting the temperature increase for OT NPs in water with increasing concentration under 808-nm laser irradiation for 4 min.

the OT NPs, which hold great promise for potential applications in PTT.

Preparation of NPs

To systematically investigate the photophysical properties and biological function of IT-OTPA and the HSP70 inhibitor APZ in cells, both compounds were encapsulated within DSPE-PEG2000, forming OTAPZ NPs. Transmission electron microscopy of the OTAPZ NPs revealed uniform spherical nanostructures with decreasing hydrodynamic diameter (Fig. 3(a)). Dynamic light scattering measurements confirmed that the NPs were well dispersed in water, showing a mean hydrodynamic diameter of 174.5 nm with a polydispersity index of 0.180, which is favorable for enhanced permeability and retention effects [30, 31] (Fig. 3(a)). Furthermore, the OTAPZ NPs exhibited a negative surface charge of −31.8 mV (Fig. S9 in the ESM). This highly negative surface charge contributes to the colloidal stability and prolonged circulation time of OTAPZ NPs *in vivo*, making them suitable for phototherapy and FLI applications [32, 33]. The UV–vis/NIR absorption/fluorescence emission spectra of the OTAPZ NPs showed an absorption region from 600 to 900 nm, with a maximum absorption at 823 nm. The absorption and emission spectra of the OTAPZ NPs exhibited a blue-shifted absorption peak, suggesting that intermolecular interactions and confinement effects within the NPs contribute to modulating their optical properties (Fig. 3(b)). To assess the stability of the OTAPZ NPs under irradiation, the NPs were irradiated with 808-nm light from 0 to 15 min, and their optical properties were compared with those of ICG (Fig. S10 in the ESM). After irradiation, the OTAPZ NPs exhibited minimal changes in absorbance and size and retained their colloidal stability over a 7-day storage period at room temperature (Figs. 3(c) and 3(d)). These findings indicate that OTAPZ NPs possess excellent optical and colloidal stability, making them potential candidates for therapeutic and imaging applications.

In Vitro PTT performance assessment

To assess the therapeutic effects of various groups, flow cytometry was used to evaluate apoptosis in 4T1 cells treated with different nanocomponents, followed by 5-min exposure to an NIR laser. The OTAPZ NPs demonstrated the highest apoptosis ratio (92.00%) compared with the other groups (Figs. 4(a) and 4(b)), including PBS (0.2%), PBS+NIR (0.63%), APZ NPs (1.43%), APZ NPs+NIR (0.89%), OT NPs (1.25%), OT NPs+NIR (60.7%), and OTAPZ NPs without NIR (3.16%), after identical laser exposure conditions.

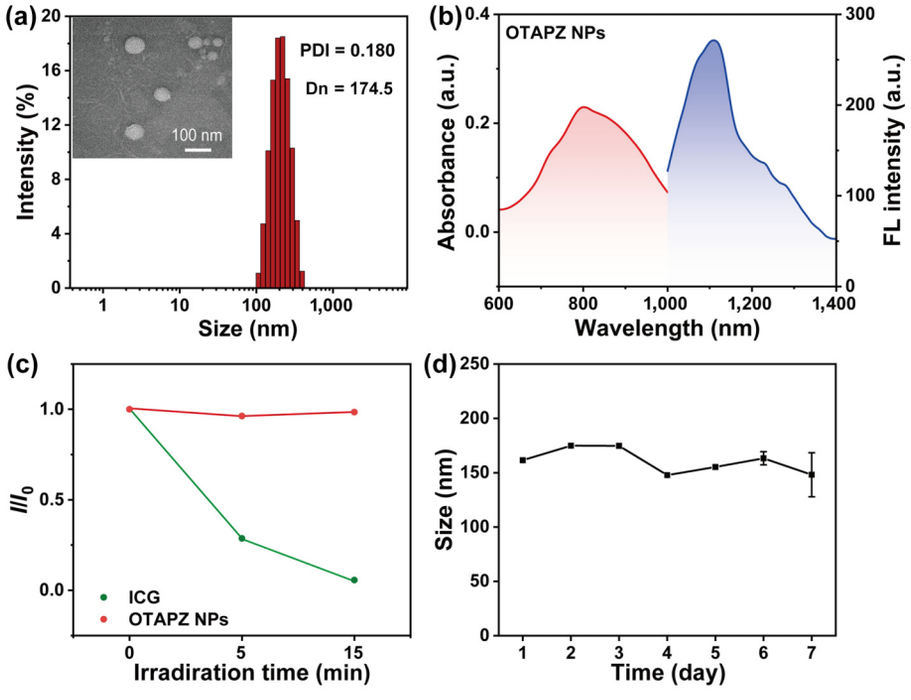

Fig. 3 (a) Representative dynamic light scattering analysis and transmission electron microscopy of OTAPZ NPs. Scale bar: 100 nm. **(b)** Normalized absorbance and fluorescence (FL) of OTAPZ NPs in water (20 μmol/L). **(c)** Absorption versus I/I_0 of OTAPZ NPs (20 μmol/L) in water under 808-nm laser irradiation for 0 min (I_0) to 15 min (n = 3). **(d)** Stability curve of OTAPZ NPs over a 7-day storage period at room temperature (n = 3).

These results indicate that the OTAPZ NPs significantly enhance the proapoptotic effect. Specifically, OTAPZ NPs induced a higher percentage of apoptosis than OT NPs, likely due to the targeted inhibition of HSP70 in the stimulated cells. In contrast, the other groups demonstrated minimal apoptosis under the absence of NIR irradiation. In addition, to demonstrate their potential therapeutic use, the biological compatibility and *in vitro* photothermal efficacy of APZ NPs, OT NPs, and OTAPZ NPs were evaluated using CCK-8 assays to gain insight into their cytotoxicity and cell viability.

As shown in Fig. 4(c), even when the concentrations of OT NPs, APZ NPs, and OTAPZ NPs increased up to 100 μmol/L, negligible cytotoxicity to 4T1 cells was observed in the absence of NIR irradiation, highlighting the excellent biosafety of the NPs (Fig. S12 in the ESM). With increasing concentrations of OTAPZ NPs under laser irradiation (808 nm, 1 W/cm^2), they exhibited a more pronounced performance than OT NPs, especially in inducing cancer hyperthermia. Live/dead cell experiments were conducted to confirm the cell-killing ability of the OTAPZ NPs (Fig. S11 in the ESM). The 4T1 cells were grown in dishes and

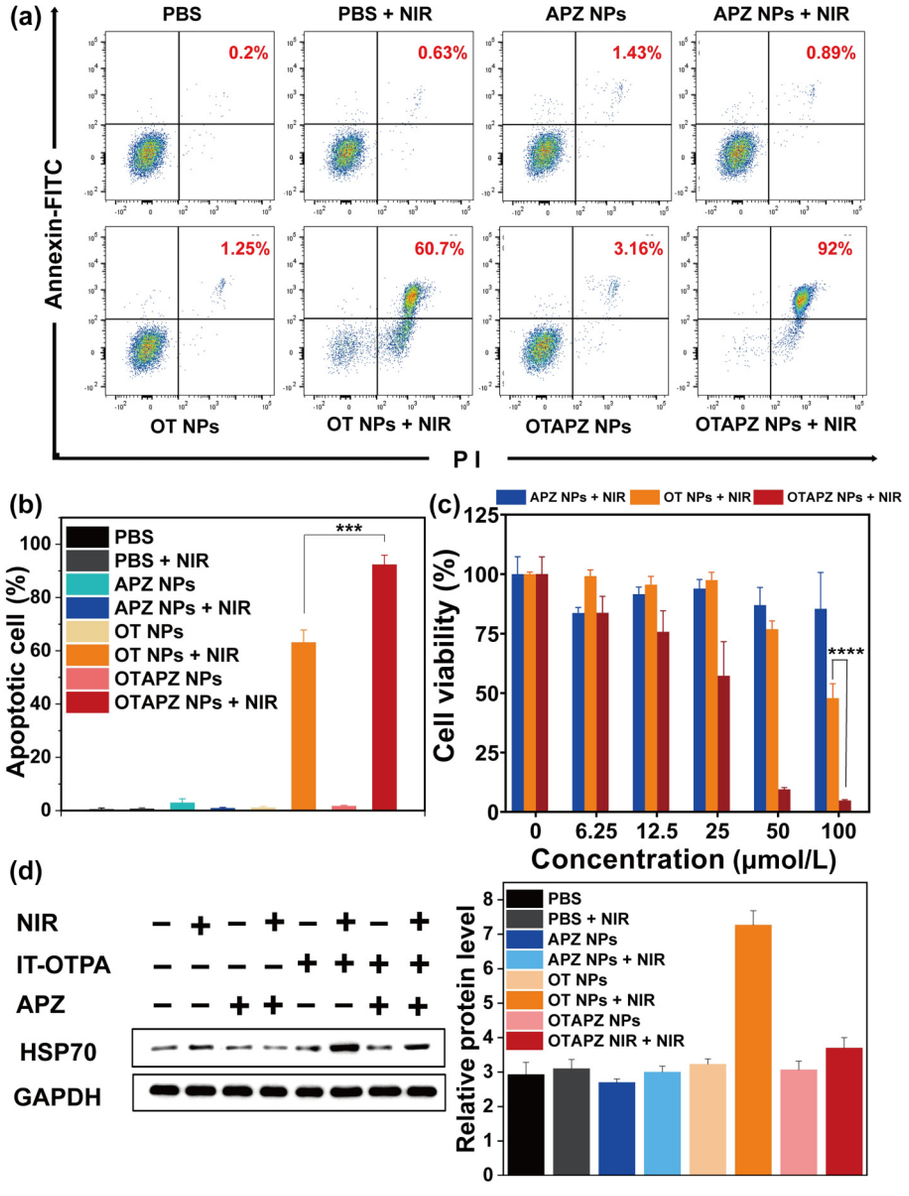

Fig. 4 (a) Apoptosis rates and **(b)** statistics of 4T1 cells after treatment with different groups, as determined via flow cytometric analysis (n = 3), ***p < 0.001. **(c)** The viabilities of 4T1 cancer cells treated with different NPs under NIR irradiation (n = 3), ****p < 0.0001. **(d)** Western blotting analysis of HSP70 expression after treatment with different formulations (n = 3). All data are presented as the mean ± standard deviation. P values were calculated using two-way analysis of variance.

cultivated for 6 h with PBS, 50 μmol/L OT NPs, APZ NPs, and OTAPZ NPs, with and without irradiation. The cells were then divided into eight groups and stained for 20 min using PI/calcein. After staining, the OTAPZ NPs+NIR group exhibited prominent red fluorescence due to PI, whereas the control groups treated with PBS, APZ NPs (with and without NIR), and OT NPs (without NIR) displayed weaker fluorescence. These results aligned with the data obtained from the CCK-8 assays, further confirming the biocompatibility and efficacy of OTAPZ NPs without irradiation. The expression of HSP70 in 4T1 cells was subsequently investigated under MTPTT conditions. Upon irradiation, a considerable increase in HSP70 expression was observed in cells treated with OT NPs, suggesting that MTPTT caused HSP70 induction (Fig. 4(d)). In contrast, the expression of HSP70 was notably reduced in cells treated with OTAPZ NPs+NIR. This reduction indicates that the HSP70 inhibitor APZ effectively suppressed HSP70 expression during MTPTT treatment, confirming the ability of APZ to inhibit HSP70 expression during the MTPTT process. Finally, treatment of MC38 and HeLa cell models with OTAPZ NPs confirmed the universality of OTAPZ NPs. In a CCK8 experiment, with increasing concentration of OTAPZ NPs from 0 to 100 μmol/L, MC38 and Hela cells showed obvious apoptosis (Fig. S16 in the ESM).

NIR-II imaging *in vivo*

The impressive brightness and PCE of OTAPZ NPs in the NIR-II window from 1 000 to 1 400 nm *in vitro* prompted us to investigate their feasibility *in vivo*. NIR-II imaging was conducted in a murine subcutaneous breast tumor model. After intravenous injection of OTAPZ NPs via the tail vein, the FLI performance of OTAPZ NPs was evaluated using a commercial imaging system under 808-nm laser irradiation. Fluorescence images of 4T1 tumor-bearing mice were recorded at 0, 0.5, 1, 2, 8, 12, and 48 h after injection (Fig. 5(a)). At the initial time point (0 h), the NIR-II FLI intensity was very weak when using a long-pass filter of 1 000 nm, minimizing the background interference. Two hours after injection, clear fluorescence signals were observed at the site of the subcutaneous 4T1 tumor. The fluorescence intensity gradually increased and peaked at 8 h, indicating that this was the optimal time point for subsequent *in vivo* phototherapy. After 8 h, the fluorescence intensity remained at a high level at the tumor site for up to 24 h (Fig. 5(b) and Fig. S13 in the ESM). At the end of the experiment, the vital organs (heart, spleen, liver, lungs, and kidneys) and the tumor were harvested for *ex vivo* FLI. Biodistribution analysis (Figs. 5(c) and 5(d)) revealed that the OTAPZ NPs predominantly accumulated at the tumor site, although the majority of the NPs were retained in the mononuclear phagocyte system (liver and spleen). This confirms that the OTAPZ NPs exhibit favorable tumor-targeting properties and remain at the tumor site for

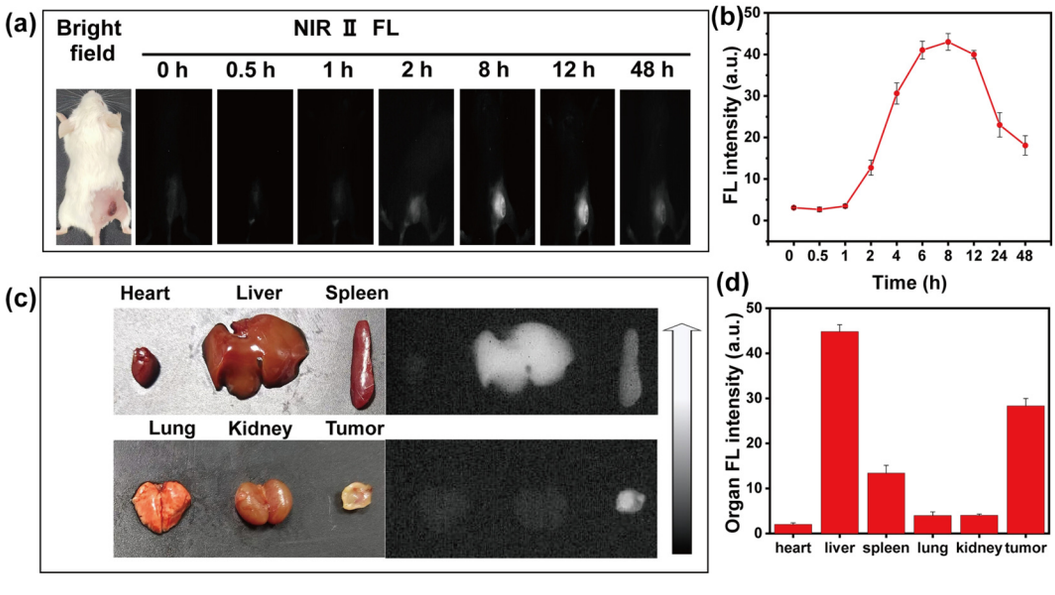

Fig. 5 (a) NIR-II fluorescence imaging of 4T1 tumor-bearing mice treated with OTAPZ NPs from 0 to 48 h (200 μL, OTAPZ concentration = 200 μmol/L). **(b)** Changes in NIR-II fluorescence intensity with time (n = 3). **(c)** NIR-II fluorescence images of the vital organs and tumor removed from the mice at 8 h. **(d)** Fluorescence intensity of the removed organs and tumor (n = 3).

an extended duration, suggesting their potential for imaging and therapeutic applications.

In vivo PTT

The capability of OTAPZ NPs for animal therapy was further assessed in 4T1 tumor-bearing mice. These mice were randomly divided into eight groups after subcutaneous inoculation of 4T1 cells. At the start of the experiment, PBS, APZ NPs, OT NPs, and OTAPZ NPs were intravenously injected into the corresponding groups (Fig. 6(a)). After 8 h, the PBS+NIR, APZ NPs+NIR, OT NPs+NIR, and OTAPZ NPs+NIR groups were subjected to irradiation (808 nm, 0.5 W/cm²) for 5 min at the tumor site. Infrared thermal images of the living mice were recorded at different time intervals to monitor the temperature changes (Fig. 6(b)). The tumors treated with PBS+NIR and APZ NPs+NIR showed little temperature increase, indicating that NIR light alone had little effect on tumor growth, which is consistent with the results of *in vitro* CCK8 assay. In contrast, a clear temperature increase was observed in the tumor regions of mice injected with OT NPs and OTAPZ NPs after laser irradiation, with the temperature reaching approximately 42 °C after 1 min of exposure. This moderate temperature is ideal for tumor inhibition while protecting the surrounding tissues. These results confirm the significant photothermal response of the OTAPZ NPs under NIR-II irradiation. Next, the therapeutic efficacy of the three types of NPs was evaluated by continuously monitoring the tumor volume for 14 days after MTPTT. As displayed in Fig. 6(c), the tumor volumes in the PBS+NIR, APZ NPs, and APZ NPs+NIR groups were similar to those in the PBS group, confirming that these treatments had negligible effects on tumor growth. In contrast, OTAPZ NPs and OT NPs significantly slowed tumor growth during the first 4 days after laser irradiation. However, only treatment with OTAPZ NPs demonstrated sustained tumor suppression over the 14-day period, whereas the effectiveness of OT NP treatment decreased with time. These results suggest that OTAPZ NPs outperform OT NPs in terms of durability of antitumor efficacy and therapeutic effect.

The body weight of each mouse was monitored

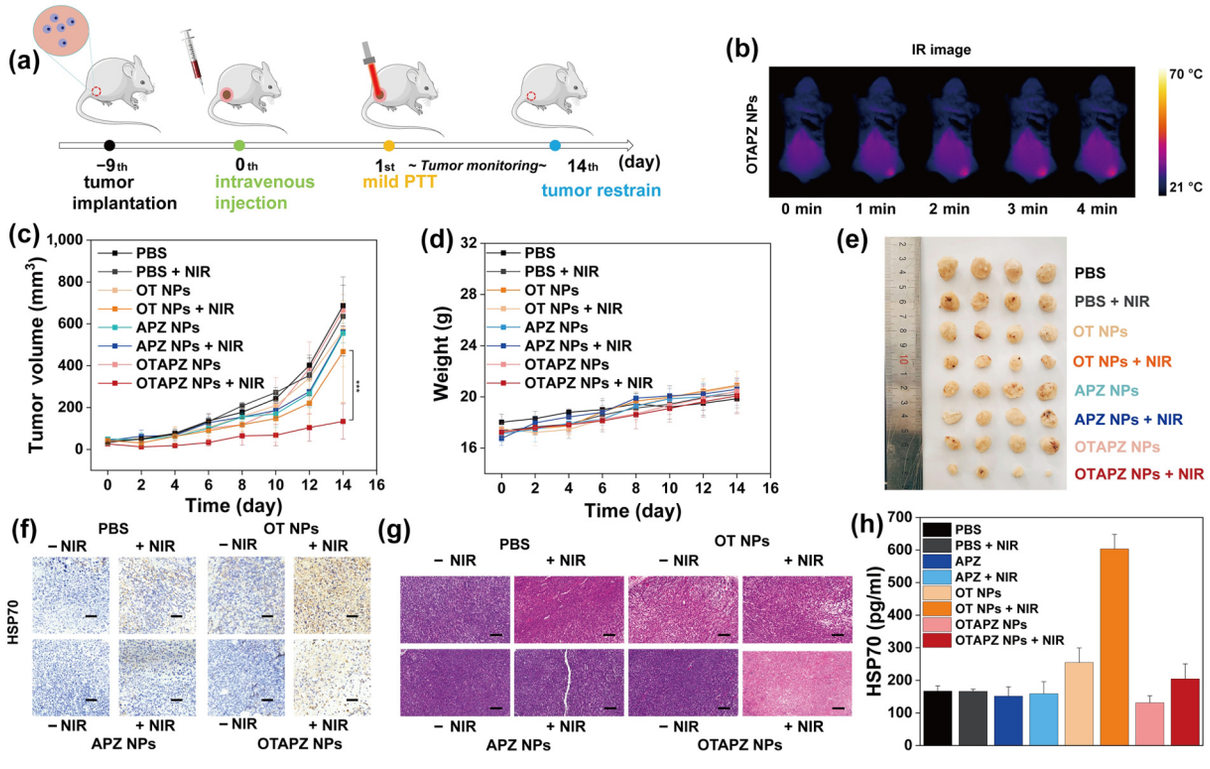

Fig. 6 (a) Mild-temperature photothermal therapy (MTPTT) procedure. **(b)** Infrared images of tumor-bearing mice treated with OTAPZ NPs + NIR captured during 4 min of irradiation. **(c)** Tumor volume after respective treatments (n = 4). **(d)** Body weight changes in tumor-bearing mice subjected to the indicated treatments (n = 4), ***p < 0.001. **(e)** Tumors removed from the mouse on day 14 after treatment. **(f)** HSP70 dyeing analysis. Scale bar: 100 μm. **(g)** Hematoxylin and eosin staining of removed tumor tissue after treatment (n = 3). **(h)** HSP 70 level of tumor tissues from different groups on day 14 after treatment (n = 3). All data are presented as the mean ± standard deviation. p values were calculated using two-way analysis of variance.

every 2 days for 14 consecutive days to examine the potential side effects of the treatments. As shown in Fig. 6(d), no significant weight reduction was observed in any group, indicating that the three NP formulations (OTAPZ NPs, OT NPs, and APZ NPs) had minimal impact on the overall health of the mice. This suggests that these NPs are biocompatible and do not induce significant toxicity during the experiment. After the 14-day observation period, all mice were euthanized, and their organs and tumors were removed for further analysis (Fig. 6(e)). To investigate the therapeutic efficacy of MTPTT, IHC analyses of tumor tissues were conducted using H&E, Ki67, and HSP70 staining. H&E staining of tumor tissue sections from the OTAPZ NPs group showed a reduction in tumor cells, indicating that MTPTT effectively reduced tumor growth. In contrast, the other groups exhibited minimal histological changes, suggesting less therapeutic impact. IHC staining for HSP70 revealed an increase in HSP70 expression with increasing temperature due to irradiation, with a marked reduction in HSP70 expression in the OTAPZ NPs+NIR group due to the effect of APZ. Ki67 staining, a marker of cell proliferation, showed higher Ki67 expression in the PBS, PBS+NIR, OT NPs, OT NPs+NIR, APZ NPs, and APZ NPs+NIR groups compared with the OTAPZ NPs+NIR group (Figs. 6(f) and 6(g) and Fig. S15 in the ESM). This indicated that MTPTT with OTAPZ NPs effectively inhibited tumor cell proliferation. In addition, statistical analysis was conducted after the tumor tissue was ground, and high levels of HSP70 were detected in the OT NPs + NIR group, whereas the other groups exhibited lower levels due to the effect of APZ or the absence of NIR irradiation. These results were consistent with the western blotting experiment, confirming the mechanism of action of OTAPZ NPs in MTPTT (Fig. 6(h)).

Histological analysis and blood biochemistry/ routine examination

To further evaluate the safety of the NPs, the PBS, APZ NPs, OT NPs, and OTAPZ NPs groups of mice were subjected to blood and serum analysis (Fig. 7(a)). The results indicated negligible differences in the blood and serum markers among all groups, suggesting that none of the treatments caused significant alterations in the blood biochemistry. Finally, histological analyses of normal tissues, including the spleen, kidneys, lung, heart, and liver, were performed using H&E staining. As shown in Fig. 7(b), no obvious damage was detected in these organs across all groups, further indicating that OTAPZ NPs, OT NPs, and APZ NPs did not cause significant toxicity or damage to normal organs, demonstrating their safety for therapeutic use.

In general, PTT faces certain application limitations, including the restricted penetration depth of infrared lasers (5–7 mm), which prevents the effective treatment of deep-seated tumors. Additionally, high-power laser irradiation may cause damage to normal skin tissues. Moreover, challenges in the delivery and conversion of photosensitizers as well as safety concerns remain critical issues in clinical applications. Furthermore, PTT requires exogenous laser devices that meet specific standards, imposing additional demands with regard to treatment facilities and equipment. To circumvent these issues, the development and optimization of materials offers a promising approach. In the field of AIE, research can focus on enhancing biocompatibility, stability, and targeted *in vivo* conversion efficiency. Moreover, as the synthesis techniques improve, the production cost of the materials is expected to decrease. The combination of reported photosensitizer materials with chemotherapy drugs also offers a promising direction for future development.

Conclusions

IT-OTPA featuring a D–A–D structure was successfully designed with furan-modified thiadiazolo-quinoxaline as a novel photothermal agent. This design enables a balanced enhancement of the PCE and FQY in the NIR-II region. The D–A–D structure optimizes the electronic properties of the dye, endowing it with efficient light absorption and photothermal conversion ability, and the incorporation of furan and thiophene groups considerably enhances the PCE without compromising the strong fluorescence emission between 1000 and 1400 nm. This dual enhancement provides not only an effective tumor treatment approach via MTPTT but also real-time imaging, making it ideal for integrated cancer therapy. By encapsulating IT-OTPA into NPs and combining the resulting OT NPs with the HSP70 inhibitor APZ to form OTAPZ NPs, an effective platform for PTT and FLI was established. The results highlight the

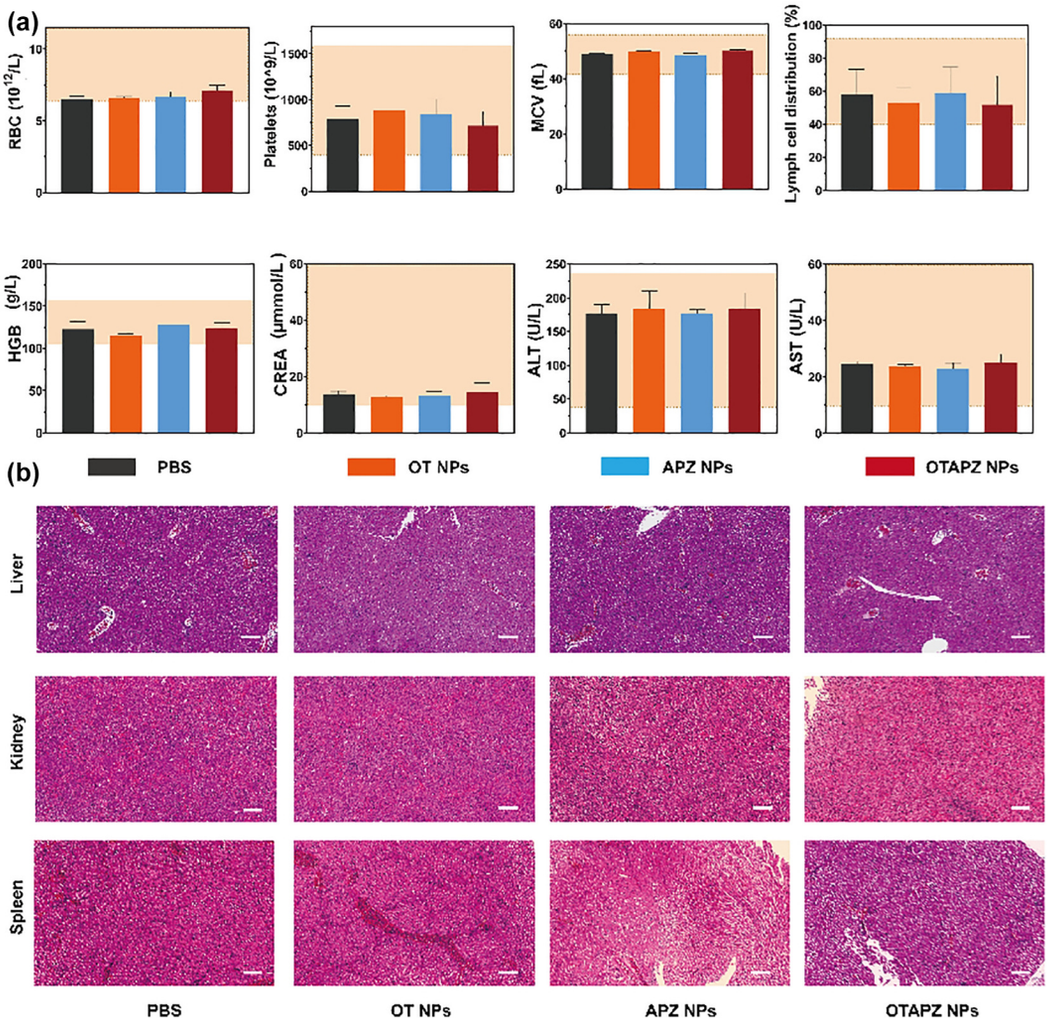

Fig. 7 (a) Blood biochemistry and blood routine of mice. The orange area indicates the normal physiological range for each indicator (n = 3). **(b)** Hematoxylin and eosin staining of the liver, spleen, kidneys (n = 3). Scale bar: 100 μm.

potential of this D–A–D structured dye, which combines high PCE for efficient tumor treatment and high FQY for precise FLI, for improving the efficiency of cancer therapy.

Ethical Approvals

All procedures involving animals were conducted in accordance with the guidelines of the Tianjin Municipal Committee for the Use and Care of Laboratory Animals, under the supervision of the Nankai University Animal Ethics Committee (Approval Number: SYXK (Jin) 2020-0007).

CRediT Author Statement

Zuyuan Zhang，**Xuan Sun, and Chunbai Xiang**: experiment section. **Tianhe Qiao, Xin Wang:** visualization, writing original draft, writing–review & editing, data curation, formal analysis, investigation, conceptualization, methodology, project administration, and supervision.

Acknowledgements

This study was partially supported by the National Natural Science Foundation of China (No. 82172835). The authors also acknowledge the Doctoral Scientific Research Foundation of Xinxiang Medical University (No. 505541).

Conflict of Interests

The authors declare no competing financial interest.

Supporting Information

Supporting information to this article can be found online at https://doi.org/10.26599/NBE.2025.9290120

References

[1] Y.C. Liu, L.L. Teng, X.F. Lou, et al. "Four-in-one" design of a hemicyanine-based modular scaffold for high-contrast activatable molecular afterglow imaging. *Journal of the American Chemical Society*, 2023, 145(9): 5134–5144. https://doi.org/10.1021/jacs.2c11466

[2] Y.J. Liu, P. Bhattarai, Z.F. Dai, et al. Photothermal therapy and photoacoustic imaging *via* nanotheranostics in fighting cancer. *Chemical Society Reviews*, 2019, 48(7): 2053−2108. https://doi.org/10.1039/C8CS00618K

[3] Q.L. Ma, X. Sun, W.L. Wang, et al. Diketopyrrolopyrrole-derived organic small molecular dyes for tumor phototheranostics. *Chinese Chemical Letters*, 2022, 33(4): 1681−1692. https://doi.org/10.1016/j.cclet.2021.10.054

[4] P.A. Schornack, R.J. Gillies. Contributions of cell metabolism and H+ diffusion to the acidic pH of tumors. *Neoplasia*, 2003, 5(2): 135−145. https://doi.org/10.1016/S1476-5586(03)80005-2

[5] H.S. Jung, P. Verwilst, A. Sharma, et al. Organic molecule-based photothermal agents: An expanding photothermal therapy universe. *Chemical Society Reviews*, 2018, 47(7): 2280−2297. https://doi.org/10.1039/C7CS00522A

[6] H.T. Chen, P.P. Bao, Y.H. Lv, et al. Enhancing NIR-II imaging and photothermal therapy for improved oral cancer theranostics by combining TICT and aggregation-induced emission. *ACS Applied Materials & Interfaces*, 2023, 15(49): 56895−56908. https://doi.org/10.1021/acsami.3c14905

[7] M. Wang, D.Y. Yan, M. Wang, et al. A versatile 980 nm absorbing aggregation-induced emission luminogen for NIR-II imaging-guided synergistic photo-immunotherapy against advanced pancreatic cancer. *Advanced Functional Materials*, 2022, 32(36): 2205371. https://doi.org/10.1002/adfm.202205371

[8] H.C. Shen, F.Y. Sun, X.Y. Zhu, et al. Rational design of NIR-II AIEgens with ultrahigh quantum yields for photo- and chemiluminescence imaging. *Journal of the American Chemical Society*, 2022, 144(33): 15391−15402. https://doi.org/10.1021/jacs.2c07443

[9] J.W. Song, X.Y. Kang, L. Wang, et al. Near-infrared-II photoacoustic imaging and photo-triggered synergistic treatment of thrombosis *via* fibrin-specific homopolymer nanoparticles. *Nature Communications*, 2023, 14: 6881. https://doi.org/10.1038/s41467-023-42691-8

[10] B. Li, M. Zhao, W. Lai, et al. Activatable NIR-II photothermal lipid nanoparticles for improved messenger RNA delivery. *Angewandte Chemie International Edition*, 2023, 62(25): e202302676. https://doi.org/10.1002/anie.202302676

[11] L. He, L.H. He, S. Xu, et al. Engineering of reversible NIR-II redox-responsive fluorescent probes for imaging of inflammation *in vivo*. *Angewandte Chemie International Edition*, 2022, 61(46): e202211409. https://doi.org/10.1002/anie.202211409

[12] G.S. Hong, A.L. Antaris, H.J. Dai. Near-infrared fluorophores for biomedical imaging. *Nature Biomedical Engineering*, 2017, 1: 0010. https://doi.org/10.1038/s41551-016-0010

[13] C.F. You, Y.Q. Zhu, J. Zhu, et al. Strength in numbers: A giant NIR-II AIEgen with one-for-all phototheranostic features for exceptional orthotopic bladder cancer treatment. *Angewandte Chemie International Edition*, 2025, 64(6): e202417865. https://doi.org/10.1002/anie.202417865

[14] Z. Zhao, H.K. Zhang, J.W.Y. Lam, et al. Aggregation-induced emission: new vistas at the aggregate leve. *Angewandte Chemie International Edition*, 2020, 59(25): 9888−9907. https://doi.org/10.1002/anie.201916729

[15] Q.Q. Li, Z. Li. Miracles of molecular uniting. *Science China Materials*, 2020, 63(2): 177−184. https://doi.org/10.1007/s40843-019-1172-2

[16] N. Jiang, T.X. Shen, J.Z. Sun, et al. Aggregation-induced emission: Right there shining. *Science China Materials*, 2019, 62(9): 1227−1235. https://doi.org/10.1007/s40843-019-9443-8

[17] S.D. Xu, Y.K. Duan, B. Liu. Precise molecular design for high-performance luminogens with aggregation-induced emission. *Advanced Materials*, 2020, 32(1): e1903530. https://doi.org/10.1002/adma.201903530

[18] S. Liu, Y. Li, J. Zhang, et al. A two-in-one Janus NIR-II AIEgen with balanced absorption and emission for image-guided precision surgery. *Materials Today Bio*, 2021, 10: 100087. https://doi.org/10.1016/j.mtbio.2020.100087

[19] L. Yuan, Y.B. Su, B. Yu, et al. D-A-D organic small molecules with AIE effect for fluorescence imaging guided photothermal therapy. *Biomaterials Science*, 2023, 11(3): 985–997. https://pubmed.ncbi.nlm.nih.gov/36541206/

[20] C. Wang, F. Wang, W.T. Zou, et al. Donor-acceptor-donor small molecules for fluorescence/photoacoustic imaging and integrated photothermal therapy. *Acta Biomaterialia*, 2023, 164: 588−603. https://doi.org/10.1016/j.actbio.2023.04.024

[21] P.P. Xiao, Y. Sun, M.K. Liang, et al. A fluorophore with dithienopyrrole donor for beyond 1300 nm NIR-II fluorescence/photoacoustic dual-model imaging and photothermal therapy. *Materials Today Nano*, 2023, 24: 100404. https://doi.org/10.1016/j.mtnano.2023.100404

[22] J. Li, R.N. Wang, Y. Sun, et al. NIR-II fluorophore with dithienylethene as an electron donor for fluorescence/photoacoustic dual-model imaging and photothermal therapy. *ACS Applied Materials & Interfaces*, 2021, 13(46): 54830−54839. https://doi.org/10.1021/acsami.1c17813

[23] G.D. Chai, J.Q. Zhang, M. Pan, et al. Deciphering the role of chalcogen-containing heterocycles in nonfullerene acceptors for organic solar cells. *ACS Energy Letters*, 2020, 5(11): 3415. https://doi.org/10.1021/acsenergylett.0c01688

[24] B. Briou, B. Améduri, B. Boutevin. Trends in the Diels–Alder reaction in polymer chemistry. *Chemical Society Reviews*, 2021, 50(19): 11055−11097. https://doi.org/10.1039/D0CS01382J

[25] R.C. Cioc, M. Crockatt, J.C. van der Waal, et al. The interplay between kinetics and thermodynamics in furan Diels-alder chemistry for sustainable chemicals production. *Angewandte Chemie International Edition*, 2022, 61(17): e202114720. https://doi.org/10.1002/anie.202114720

[26] Z.L. Cao, M.Y. Wang, H.M. Gao, et al. Porous organic polymers *via* Diels-alder reaction for the removal of Cr(VI) from aqueous solutions. *ACS Macro Letters*, 2022, 11(4): 447−451. https://doi.org/10.1021/acsmacrolett.2c00052

[27] Y.X. Xu, C.C. Chueh, H.L. Yip, et al. Improved charge transport and absorption coefficient in indacenodithieno [3, 2-b] thiophene-based ladder-type polymer leading to highly efficient polymer solar cells. *Advanced Materials*, 2012, 24(47): 6356−6361. https://doi.org/10.1002/adma.201203246

[28] S.L. Li, X.Y. Wang, R. Hu, et al. Near-infrared (NIR)-

absorbing conjugated polymer dots as highly effective photothermal materials for *in vivo* cancer therapy. *Chemistry of Materials*, 2016, 28(23): 8669−8675. https://doi.org/10.1021/acs.chemmater.6b03738

[29] X.G. Guo, N.J. Zhou, S.J. Lou, et al. Bithiopheneimide-dithienosilole/dithienogermole copolymers for efficient solar cells: Information from structure-property-device performance correlations and comparison to thieno [3, 4-c] pyrrole-4, 6-dione analogues. *Journal of the American Chemical Society*, 2012, 134(44): 18427−18439. https://doi.org/10.1021/ja3081583

[30] X.H. Gao, Y.Y. Cui, R.M. Levenson, et al. M. *In vivo* cancer targeting and imaging with semiconductor quantum dots. *Nature Biotechnology*, 2004, 22(8): 969−976. https://doi.org/10.1038/nbt994

[31] L. Cheng, W.W. He, H. Gong, et al. PEGylated micelle nanoparticles encapsulating a non-fluorescent near-infrared organic dye as a safe and highly-effective photothermal agent for *in vivo* cancer therapy. *Advanced Functional Materials*, 2013, 23(47): 5893−5902. https://doi.org/10.1002/adfm.201301045

[32] B.W. Yang, Y. Chen, J.L. Shi. Tumor-specific chemotherapy by nanomedicine-enabled differential stress sensitization. *Angewandte Chemie International Edition*, 2020, 59(24): 9693−9701. https://doi.org/10.1002/anie.202002306

[33] Q. Cheng, T.W. Li, Y.L. Tian, et al. NIR-II fluorescence imaging-guided photothermal therapy with amphiphilic polypeptide nanoparticles encapsulating organic NIR-II dye. *ACS Applied Bio Materials*, 2020, 3(12): 8953−8961. https://doi.org/10.1021/acsabm.0c01218